

Dynamic Channel Modeling for Mode-Division Multiplexing

Karthik Choutagunta, *Student Member, IEEE*, and Joseph M. Kahn, *Fellow, IEEE*

Abstract—Environmental perturbations, such as wind, mechanical stress, temperature, and lightning, impose microsecond-time-scale changes to the transfer matrix of a multimode fiber (MMF), necessitating adaptive multiple-input multiple-output (MIMO) equalization to track the time-varying channel. It is of significant interest to accurately model channel dynamics so that adaptive MIMO equalization algorithms can be optimized and their impact on digital signal processing complexity and performance can be assessed. We propose a dynamic channel model using coupled-mode theory to describe time-varying polarization- and spatial-mode coupling in MMF caused by fast environmental perturbations. Our method assumes that the MMF has built-in refractive index and geometric defects that are responsible for random birefringence and mode coupling. Various time-varying perturbations modify the coupling coefficients in the coupled-mode equations to drive channel dynamics. We use our dynamic channel model to simulate an example aerial fiber link subject to a sudden gust of wind and show that increasing the strength of the perturbation, the number of modes, and the length of exposed fiber all lead to higher error at the output of an adaptive MIMO equalizer. We employ the model to study the convergence and tracking performance of the least-mean-squares adaptive equalization algorithm.

Index Terms—Dynamic channel models, environmental perturbations, equalization, MIMO, modal dispersion, mode coupling, mode-division multiplexing, receiver signal processing, tracking.

I. INTRODUCTION

AS THE throughput of single-mode fiber (SMF) systems approach information-theoretic capacity limits imposed by amplifier noise and fiber nonlinearities, mode-division multiplexing (MDM) in multi-mode fiber (MMF) offers a new way of supporting continued traffic growth [1]. A form of multi-input multi-output (MIMO) transmission, MDM exploits spatial degrees of freedom by launching modulated data signals onto D orthogonal spatial and polarization waveguide modes. If all the degrees of freedom that are used to increase data rates in SMF ($D = 2$), such as time/frequency, quadrature phase and polarization, are used in each mode of a MMF, then the capacity per fiber ideally increases proportionally to D .

However, random distributed perturbations to the fiber geometry and index profile along the link break the orthogonality

Manuscript received September 16, 2016; revised December 24, 2016 and January 13, 2017; accepted January 17, 2017. Date of publication January 22, 2017; date of current version April 20, 2017. This work was supported by Huawei Technologies Co., Ltd., and in part by a Stanford Graduate Fellowship.

The authors are with the E. L. Ginzton Laboratory, Department of Electrical Engineering, Stanford University, Stanford, CA 94305 USA (e-mail: kchoutag@stanford.edu; jmk@ee.stanford.edu).

Color versions of one or more of the figures in this paper are available online at <http://ieeexplore.ieee.org>.

Digital Object Identifier 10.1109/JLT.2017.2656821

between modes, causing them to couple to each other. Modal dispersion (MD), arising from different group velocities of the propagating modes, spreads the transmitted data in time, leading to intersymbol interference. Mode-dependent loss (MDL), arising from the fiber and from inline components, such as multimode erbium-doped fiber amplifiers (MM-EDFAs), interacts with random mode coupling to create a non-unitary channel, which cannot be inverted at the receiver without incurring a penalty [2]. Environmental perturbations disturb the fiber channel, causing mode coupling and dispersion to change on the microsecond time scale [3]–[9].

Long-haul MDM systems typically employ an adaptive MIMO frequency domain equalizer (FDE) at the receiver to compensate for modal crosstalk and MD. Efficient realization of a MIMO FDE using the fast Fourier transform (FFT) requires an overhead in the form of a cyclic prefix (CP) [10]. The large group delay spread inherent in long-haul MDM links necessitates a long CP, and in order to achieve a high CP efficiency, the FFT block length must be large compared to the CP length. Even if the adaptive MIMO FDE uses overlap convolution instead of a CP, its computational complexity is minimized by using an FFT block length that is long compared to the channel delay spread [11]. Using a long FFT block length, however, slows down the equalizer's convergence and tracking ability. Accurate dynamic models to describe temporal channel variations are needed to study this critical tradeoff in MDM systems.

Much of the existing literature on channel models has focused on the static aspects of modal propagation. For SMFs, there are numerous statistical models describing changes to the state of polarization (SOP) or polarization mode dispersion (PMD) as the frequency or fiber length is varied [12]–[14]. For MMFs, the weak coupling between linearly polarized mode groups was studied in [15] and the evolution of modal dispersion with length and frequency was modeled using the generalized Stokes space in [16]. To date, the treatment of dynamic effects has been restricted to the hinge model of PMD in SMF [5], [14], [17]–[24]. The hinge model is an extension of the wave plate model, which treats a long SMF as a concatenation of birefringent elements with random differential group delays (DGDs) and mode coupling angles [14]. PMD dynamics are dominated by a small number of exposed hinges that randomly rotate the SOP on the Poincaré sphere. While it is not entirely clear what physical processes are responsible for channel dynamics, some authors have tried to relate fast polarization dynamics to twist in aerial cables [21] and axial stress

across spooled fibers [25]. There has yet to be a comprehensive theory explaining the nature of dynamic mode coupling, even in SMF.

Several challenges are encountered in trying to extend the hinge model to describe mode coupling dynamics in MMFs. One challenge relates to dimensionality. SMFs support only $D = 2$ degrees of freedom, which are fully coupled in long fibers. A model providing full coupling may fit experimental observations even if the model is based on simplified physical assumptions. By contrast, MMFs support $D > 2$ degrees of freedom, which are not equally coupled in general. A model incorporating a detailed description of the underlying physics is likely required to fit experimental observations. Another challenge is that modeling MDM channel dynamics for $D > 2$ is non-trivial in generalized Stokes space. Not all vectors on the generalized Poincaré sphere have a valid Jones representation [16], and so rotations on the generalized Poincaré sphere can be non-physical. Finally, perhaps the greatest challenge at present is the lack of extensive field measurements of installed MMFs. Initial experiments have suggested that mechanical perturbation can possibly change MD in MMFs an order of magnitude faster than PMD in SMFs owing to increased degrees of freedom [6].

Our dynamic channel model attempts to address the aforementioned concerns. While the traditional hinge model for SMF assumes that PMD dynamics is dominated by localized birefringent elements surrounded by localized polarization-changing hinges, our model can include perturbations that are either localized or distributed. Our model employs coupled mode differential equations that are valid for all D . The solution of these equations is approximated by numerical integration, and distributed effects can be modeled well if the step size is chosen to be sufficiently small.

Our model assumes that the fiber has built-in birefringence and mode coupling due to refractive index and geometric defects that are frozen during manufacturing or cabling, and the coefficients in the coupled mode equations are chosen such that the behavior of the fiber predicted by our model is consistent with experimental observations of static fibers. We use perturbation theory to derive from first principles the time-varying modifications to the coupling coefficients caused by various physical effects, including stress and curvature. To the best of our knowledge, this paper is the first physically based channel model for describing dynamic events in a general MDM system supporting D modes. Our method has the advantage of being based in the generalized Jones space, which allows us to evaluate the tracking behavior of adaptive MIMO equalizers.

The remainder of the paper is as follows. Section II presents a linear MIMO channel model for MDM systems that can describe both static and dynamic perturbations. Section III presents the low-order perturbation theory used to derive the effects of the drivers of channel dynamics. Section IV describes the modeling of an exemplary long-haul system with sections of exposed aerial fibers experiencing a sudden gust of wind. Section IV also discusses optimization of the adaptive MIMO FDE. Section V presents our conclusions.

TABLE I
SOURCES OF CHANNEL DYNAMICS IN A VARIETY OF FIBER
DEPLOYMENT SCENARIOS

Perturbation	Link Type				
	Spooled DCF	Buried link	Aerial link	Data center link	Submarine link
Maintenance	✓	✓	✓	✓	✓
Vehicular traffic		✓			
Wind gusts			✓		
Lightning strikes			✓		
Power line currents		✓	✓		✓
Seismic activity		✓			✓
Temperature	✓	✓	✓	✓	✓
Cooling fans				✓	

II. DYNAMIC CHANNEL MODEL FOR MDM

In this section, we provide the theoretical framework to model MDM channel dynamics. In Section II-A, we discuss the sources of channel dynamics in different settings. In Section II-B, we use the multi-section modeling approach to describe a point-to-point MDM link as a concatenation of static and active sections. We describe the construction of the transfer matrices of active sections using coupled mode theory. The main idea is to model the matrix of coefficients in the coupled-mode equations as the sum of a static matrix and a perturbing dynamic matrix. We describe the modeling of the static matrix in Section II-C, and then describe the modeling of the dynamic matrix in Section II-D. In Section II-E, we discuss the numerical integration of the coupled mode equations to yield a time-varying Jones matrix.

A. Environmental Perturbations in Different Link Types

As shown in Table I, deployed fiber systems are subject to several environmental disturbances, including vehicular traffic, wind, lightning strikes, and temperature changes. Depending on how a fiber link is deployed, some of the environmental perturbations will have a more significant effect on the channel than others. For example, it is reasonable to expect that aerial fibers will be affected mainly by wind gusts [26], [27] and/or lightning strikes [28], [29]. Buried fibers in terrestrial links are more shielded from the environment and will be affected mainly by vibrations arising from trains and vehicular traffic [30], [31]. Systems using spooled dispersion-compensating fibers are subject to fast dynamics because a mechanical or thermal disturbance to a spool can create a perturbation that is correlated over a long fiber length [32]. Data center links can be mechanically perturbed during server maintenance, by vibrations from rack equipment, or by changing temperature gradients during operation [33], but are more stable than long-haul links because there are fewer potential perturbations along a short link. Submarine links spanning several thousands of kilometers can be affected by maintenance, seismic activity or temperature gradients. Even though the magnitude of each perturbation might be small, these links are sufficiently long to allow distributed effects to produce noticeable changes in the end-to-end channel. It is important to characterize how the fiber channel will change in each case to evaluate the implications for MIMO equalization.

B. Multisection Modeling of a Dynamic MDM Link

We consider a general long-haul MDM link in a MMF supporting D modes. We describe the fiber as a concatenation of many independent sections. Some sections, described by a transfer matrix $\mathbf{M}_i^s(\Omega)$, are static. Others, described by $\mathbf{M}_i^d(\Omega, t)$, are dynamic, owing to interaction with a time-varying environment. Our model is an extension of the multi-section model proposed previously for MDM, since end-to-end linear propagation at each frequency Ω is described by a matrix multiplying complex baseband envelopes

$$\mathbf{M}(\Omega, t) = \prod_{i=1}^N \mathbf{M}_i^{(s,a)}(\Omega, t), \quad (1)$$

where N is the total number of sections. The time-varying transfer matrices of the active hinge sections control the overall channel dynamics.

The $D \times D$ propagation matrices of the static sections can be written using the singular value decomposition as

$$\mathbf{M}_i^s(\Omega) = \mathbf{U}_i \mathbf{\Lambda}_i(\Omega) \mathbf{V}_i^H, \quad (2)$$

where \mathbf{U}_i and \mathbf{V}_i are frequency-independent random $D \times D$ unitary matrices representing mode coupling and

$$\begin{aligned} \mathbf{\Lambda}_i(\Omega) = \text{diag} \left[\exp \left(\frac{g_{1,i}}{2} - j(\Omega - \Omega_0) \beta_{1,i}^{(1)} l_i \dots \right. \right. \\ \left. \left. - \frac{j}{2} (\Omega - \Omega_0)^2 \beta_{1,i}^{(2)} l_i \right), \dots, \exp \left(\frac{g_{D,i}}{2} \dots \right. \right. \\ \left. \left. - j(\Omega - \Omega_0) \beta_{D,i}^{(1)} l_i - \frac{j}{2} (\Omega - \Omega_0)^2 \beta_{D,i}^{(2)} l_i \right) \right] \quad (3) \end{aligned}$$

is a diagonal matrix representing mode-dependent effects, where $\mathbf{g}_i = [g_{1,i}, \dots, g_{D,i}]$ specifies the uncoupled modal gains, $\beta_i^{(1)} = [\beta_{1,i}^{(1)}, \dots, \beta_{D,i}^{(1)}]$ specifies the uncoupled group delays per unit length, $\beta_i^{(2)} = [\beta_{1,i}^{(2)}, \dots, \beta_{D,i}^{(2)}]$ specifies the uncoupled mode-dependent CD per unit length, Ω_0 is the carrier frequency and l_i is the section length.

In the following subsections, we now show how to construct the transfer Jones matrices of our dynamic channel model.

C. Coupled Mode Theory: Static Effects

In the absence of noise and nonlinearities, the propagation of D spatial and polarization modes along the z direction is given by a linear differential equation [34]

$$\frac{\partial \tilde{\mathbf{y}}(z)}{\partial z} = (-j\mathbf{\Gamma}_s(z) + \mathbf{K}_s(z)) \tilde{\mathbf{y}}(z), \quad (4)$$

where

$$\tilde{\mathbf{y}} = [y_1, y_2, \dots, y_D]^T \quad (5)$$

is a $D \times 1$ vector of complex baseband modal envelopes. To maintain consistency of notation throughout this paper, we order the modes in $\tilde{\mathbf{y}}$ in terms of increasing propagation constant. Modes having degenerate propagation constants form groups, and appear contiguously. The matrix

$$\mathbf{\Gamma}_s = \text{diag}(\beta_1, \beta_2, \dots, \beta_D) \quad (6)$$

is a $D \times D$ diagonal matrix of propagation constants and \mathbf{K}_s is a $D \times D$ skew-Hermitian matrix describing random mode coupling. Throughout this paper, we refer to $-j\mathbf{\Gamma} + \mathbf{K}$ as the mode coupling coefficient matrix.¹

The propagation constants are modeled as

$$\begin{aligned} \beta_{i,x}(z) &= jg_i(z) + \beta_{i,x}^{(0)} + (\Omega - \Omega_0) \beta_{i,x}^{(1)}(z) \\ &\quad + \frac{1}{2} (\Omega - \Omega_0)^2 \beta_{i,x}^{(2)}(z) \\ &= \beta_{i,y}(z) + b_i(z), \end{aligned} \quad (7)$$

where $\beta_i^{(0)}$ are the phase shifts per unit length and b_i are the birefringences between x and y polarizations. The elements of \mathbf{K}_s describe pair-wise mode coupling according to [34]

$$K_{s,ij}(z) = -\frac{j\Omega}{4} \iint \psi_i^* \Delta \epsilon(z) \psi_j dA = -K_{s,ij}^*(z), \quad (8)$$

where ψ_i and ψ_j are the spatial mode field patterns of modes i and j respectively, and $\Delta \epsilon(z)$ is a transverse perturbation to the ideal refractive index profile that is responsible for mode coupling.

The mode coupling coefficients $K_{s,ij}(z)$ are, in general, complex-valued random processes that vary along the propagation distance due to various uncontrolled sources, such as core non-circularity, core radius variations, roughness at the core-cladding boundary, macro- and micro-bends, twists, cabling-induced stresses, and so on. To emulate this behavior in our simulations, we have assumed that $K_{s,ij}$ are complex random processes that evolve according to Langevin equations [35]

$$\frac{\partial K_{s,ij}}{\partial z} = -\frac{K_{s,ij}}{L_c} + g_{ij}(z), \quad (9)$$

where L_c is a mode coupling correlation length and $g_{ij}(z)$ are proper complex white noise processes that satisfy

$$\mathbb{E} [g_{ij}^*(z) g_{i'j'}(z')] = \frac{\sigma_{K_{s,ij}}^2}{L_c} \delta(z - z') \delta(i - i') \delta(j - j'), \quad (10)$$

$$\mathbb{E} [g_{ij}(z) g_{i'j'}(z')] = 0. \quad (11)$$

The real and imaginary parts of $K_{s,ij}$ are uncorrelated because the pseudocovariance of $g_{ij}(z)$ is zero in (11) [36].

Phase matching conditions imply that modes with nearly equal propagation constants couple more strongly than modes with highly unequal propagation constants. The strength of the pairwise mode coupling depends on the beat length $L_{B,ij} = 2\pi/|\beta_i - \beta_j|$. Previous studies of mode coupling in MMFs [37], [38] showed that the strength of mode coupling scales super-linearly with the beat length. In our simulations, we have assumed that $\sigma_{K_{s,ij}}^2$ scales with the fourth power of $L_{B,ij}$.

¹The MDM research community often uses the term ‘‘coupling matrix’’ to describe both the transfer matrix and the exponent of the transfer matrix interchangeably. To avoid this confusion, we call $-j\mathbf{\Gamma} + \mathbf{K}$ the ‘‘mode coupling coefficient matrix’’ since it is an efficient way to represent the coefficients in the system of coupled-mode differential equations. Terms with subscripts s and d describe static and dynamic effects, respectively. In general, the mode coupling coefficient matrix can contain both diagonal and off-diagonal elements and, as will be evident later, the model can produce a time-varying Jones transfer matrix even if the dynamic mode coupling coefficient matrix is purely diagonal.

TABLE II
SUMMARY OF PHYSICAL EFFECTS IN THE DYNAMIC CHANNEL MODEL

Driver of Channel Dynamics	Propagation Constant	Mode Coupling	Geometry
Axial Stress T_{zz}	$\Delta\beta_i = -\frac{1}{2} \left(\frac{k_0^2(p_{12} - \sigma(p_{11} + p_{12}))}{\beta_i} \right)$ $\times \left(\frac{\int \int n_0^4 \psi_i ^2 dA}{\int \int \psi_i ^2 dA} \right) \left(\frac{T_{zz}}{Y} \right)$ $\Delta b_i = \left(\frac{-k_0 n_0^3 (p_{11} - p_{12})(1 + \sigma)}{4} \right)$ $\times \left(\frac{a}{R} \right) \left(\frac{2(2 - 3\sigma)}{1 - \sigma} \right) \left(\frac{T_{zz}}{Y} \right)$	$\Delta K_{ij} = \gamma K_{ij,0} \cdot T_{zz}$	$\Delta l = \Delta l_0 \left(1 + \frac{T_{zz}}{Y} \right)$ We neglect core diameter shrinkage due to Poisson effect
Local Curvature R	$\Delta b_i = -\frac{\Omega^2 \mu_0 \varepsilon_0 n_{av}^4}{4\beta_i} \left(\frac{a}{R} \right)^2 (1 + \sigma)(p_{12} - p_{11})$	$\Delta K_{ij} = -\frac{j\Omega \varepsilon_0 n_0^2}{2R} \int \int x \psi_i^* \psi_j dA.$	Transform time-varying curvatures into equivalent straight MMF None
External Electromagnetic Fields E_{elec}, H_{mag}	$\Delta b_i = 2\pi B_K E_{elec} ^2$	$\Delta K_{ij} = V H_{mag} $ (Polarization coupling only)	None

The built-in birefringence between orthogonal polarizations manifests as a difference in propagation constant

$$b_i = \beta_{i,x} - \beta_{i,y} = k\Delta n, \quad (12)$$

Here, we have assumed that $\mathbb{E}[\Delta n/n] \approx 10^{-7}$, which is a typical value of birefringence in SMFs [35].

D. Coupled Mode Theory: Dynamic Effects

Time-varying environmental perturbations disturb the local MMF properties, and equation (4) must be modified to

$$\begin{aligned} \frac{\partial \tilde{\mathbf{y}}(z, t)}{\partial z} &= (-j\mathbf{\Gamma}_s(z) + \mathbf{K}_s(z))\tilde{\mathbf{y}}(z, t) \\ &+ (-j\mathbf{\Gamma}_d(z, t) + \mathbf{K}_d(z, t))\tilde{\mathbf{y}}(z, t) \\ &= (-j\mathbf{\Gamma}(z, t) + \mathbf{K}(z, t))\tilde{\mathbf{y}}(z, t), \end{aligned} \quad (13)$$

where the perturbing dynamic matrices $\mathbf{\Gamma}_d(z, t)$ and $\mathbf{K}_d(z, t)$ are a function of the local properties of the fiber at location z and the environmental perturbation. In the most general form, the dynamic mode coupling coefficient matrix modifies (i) the propagation constants resulting in time-varying mode-dependent phase shifts, (ii) the mode coupling coefficients resulting in time-varying mode coupling, and (iii) the geometry including the local curvature and differential section lengths (due to stress effects) resulting in modulation of both (i) and (ii). The functional dependence of the terms in the dynamic mode coupling coefficient matrix on the fiber properties and environmental effects are derived using perturbation theory, which is discussed in more detail in Section III.

E. Computing the End-to-End Jones Transfer Matrix

The transfer Jones matrix of the link can be found by solving (13). If $\mathbf{\Gamma}$ and \mathbf{K} do not have any z -dependence, then the transfer matrix of each section can be found using a matrix exponential

$$\mathbf{M}_i(\Omega, t) = e^{(-j\mathbf{\Gamma}(\Omega, t) + \mathbf{K}(\Omega, t))l_i(t)}, \quad (14)$$

where $l_i(t)$ is the length of section i at time t . However, in general $\mathbf{\Gamma}$ and \mathbf{K} are z -dependent, and computation of $\mathbf{M}_i(\Omega, t)$ involves dividing a long section into many short lengths over

TABLE III
KEY PARAMETERS IN THE DYNAMIC CHANNEL MODEL

Symbol	Quantity
$n(r)$	refractive index
a	core radius
dn/n	birefringence
$\beta^{(0)}$	propagation constants
$\beta^{(1)}, \beta^{(2)}$	modal and chromatic dispersion
D	number of propagating modes
$\lambda_{lame}, \mu_{lame}$	Lamé's parameters
Y	Young's modulus
B_K	Kerr's constant
V	Verdet's constant
σ	Poisson's ratio
p_{11}, p_{12}	elasto-optic coefficients
L_c	mode coupling correlation length
σ_{Kij}^2	mode coupling strength
$T_{zz, max}$	fused silica tensile yield stress
τ	time scale of perturbation
$R(z, t)$	local curvatures
$T_{zz}(z, t)$	axial stresses
$E_{elec}(z, t)$	external transverse electric fields
$H_{mag}(z, t)$	external axial magnetic fields
L_H	length of the hinge

which $\mathbf{\Gamma}$ and \mathbf{K} can be considered constant, applying (14) to each section, and multiplying together the resulting matrices.

III. PERTURBATIVE MODELING OF DYNAMICS

In this section, we consider the physical effects of axial stress, local curvature, and external electromagnetic fields to derive the additive perturbation terms in the dynamic mode coupling coefficient matrix $-j\mathbf{\Gamma}_d + \mathbf{K}_d$. The effects are summarized in Table II and the main physical parameters used in our channel model are summarized in Table III.

A. Environmental Effects Modeled

We begin with a quick overview of the environmental perturbations responsible for fast temporal changes in an MDM channel and discuss why our model includes certain effects but neglects others. Consider the sources of channel dynamics that affect a deployed link, which are in Table I. It is apparent that

underlying these sources are different physical mechanisms that ultimately drive channel dynamics.

Mechanical stress is expected to be an important effect whenever the MMF is subject to motion or vibration. Stress can change the fiber index profile and the geometry via elasto-optic effects [39]. Its impact on modal propagation has been widely studied in the context of fiber-based sensing [40]. We have adapted well-known results on elasto-optic effects in our work (see Section III-B).

Fiber bends can either be intentional (as in the case of spooled fibers), or unintentional (for example, when a mechanical force causes an otherwise straight fiber to deform). Aerial fibers are particularly prone to time-varying bending in the presence of wind gusts. Effects of micro- and macro-bends have also been studied widely in optical communication literature [41]–[43], where it was seen that bending leads to additional mode coupling and birefringence. A dynamic channel model would be incomplete without including bending, and for that reason, we analyze it in Section III-C.

An important source of fast polarization coupling in aerial optical fibers is Faraday rotations arising from power lines and lightning strikes. Magnetic fields emanating from nearby lightning strikes or electrical current flowing through metallic strands wrapped around aerial fibers in overhead ground wires of power transmission cables can potentially impart hundreds of thousands of rotations per second of the SOP on the Poincaré sphere [44], [45]. As shown in Fig. 3, the z -component of an induced external magnetic field interacts with the fields of the propagating modes to produce a Faraday rotation. Also, strong electric fields can be induced in the core of an aerial fiber during a lightning strike, creating linear birefringence. However, this effect is much weaker than Faraday rotation because the Kerr constant of fused silica is very weak.

The effects of external electromagnetic fields on signal propagation in SMFs and their implications for receiver DSP design has been well-studied in [44], but to the best of the authors' knowledge, there are no comparable studies existing for MMFs. Nevertheless, we attempt to model the effects of both electric and magnetic fields in Section III-D by extending SMF results in literature to the case of multiple modes.

We do not include the effects of ambient temperature in our dynamic channel model. Measurements of SOP changes in legacy SMF systems show that PMD is a strong function of temperature because changes in temperature from day to night are roughly aligned in time with DGD spectral evolution [46]. This implies that modal dispersion is also a function of temperature, although there exist few experimental results to quantify the dependence. However, in almost all practical scenarios, temperature evolves on the time scale of minutes, which is very slow compared to the symbol rate of the MDM system. Changes in the MDM channel due to temperature are thus unlikely to affect MIMO equalizer tracking.

We do not include the effects of fiber twists in our dynamic channel model. When a fiber is twisted, shear stresses exerted on the silica change its permittivity tensor via the elasto-optic effect. While it is reasonable to assume that a time-varying twist will lead to channel dynamics [21], there is relatively

little known about how twist affects spatial and polarization coupling in MMFs. This contrasts with twist in SMFs; [47] gives an in-depth overview of twist-induced polarization coupling in SMFs. The effects of twist in MMFs are treated in a recent work [48]. Owing to the lack of experimental validation, and significant uncertainty about how to model an inhomogeneous, time-varying twist (e.g., in an aerial fiber blowing in the wind), we have chosen not to include twist effects in our current work.

Finally, Berry's phase effect can induce polarization changes to any light whose propagation path is not confined to a plane [49], [50]. This effect may potentially impart fast changes to an MDM channel whenever the MMF is disturbed, but we do not consider it here because it is difficult to model and simulate correctly.

B. Modeling Axial Stress

We assume stress is coupled into the MMF as a result of environmental perturbations. Positive stress (tension) decreases the refractive index while negative stress (compression) increases it due to local density changes. We limit our analysis to axial stress T_{zz} (i.e. stress oriented along the direction of modal propagation) because we believe that axial stresses are correlated over longer distances in the z direction than transverse stresses.

As in [51], we begin with the Helmholtz equation for the transverse part of mode fields:

$$[\Delta_{\perp} + k_0^2 n_0^2 - \beta_i^2] \psi_i = 0 \quad i = 1, \dots, D. \quad (15)$$

Axial stress perturbs the squared index profile from n_0^2 to $n_0^2 + g$, causing the propagation constants to change from β to $\beta + \Delta\beta$. Equation (15) becomes

$$[\Delta_{\perp} + k_0^2 (n_0^2 + g) - (\beta_i + \Delta\beta_i)^2] \psi_i = 0. \quad (16)$$

Note that we have assumed that the propagation constants change but the mode fields ψ remain the same, which is a standard assumption in perturbation theory. Expanding and rearranging (16), we get

$$\underbrace{[\Delta_{\perp} + k_0^2 n_0^2 - \beta_i^2]}_{=0} \psi_i + \left[k_0^2 g - 2\beta_i \Delta\beta_i - \underbrace{\Delta\beta_i^2}_{\approx 0} \right] \psi_i = 0 \quad (17)$$

and after simplifying and neglecting second-order terms, we get

$$[k_0^2 g - 2\beta_i \Delta\beta_i] \psi_i = 0. \quad (18)$$

Solving (18) for the correction to the propagation constants yields

$$\Delta\beta_i = \frac{k_0^2 \iint g |\psi_i|^2 dA}{2\beta_i \iint |\psi_i|^2 dA}. \quad (19)$$

Now, we relate the axial stress to $\Delta\beta_i$ by noting that

$$g = (n_0 + \Delta n)^2 - n_0^2 \approx 2n_0 \Delta n \quad (20)$$

for small Δn . Using the well-known relationship for stress-induced change to the refractive index profile [52]

$$\Delta n = -\frac{1}{2} n_0^3 (p_{12} - \sigma (p_{11} + p_{12})) \frac{T_{zz}}{Y}, \quad (21)$$

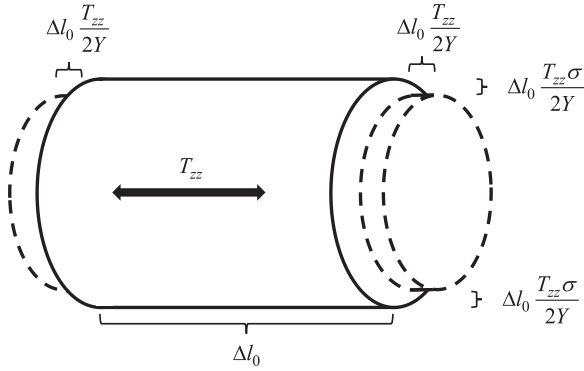


Fig. 1. The geometric effects of axial stress, which include length elongation and reduction of core diameter.

we finally obtain the stress-induced perturbation to the propagation constants

$$\Delta\beta_i = -\frac{1}{2} \left(\frac{k_0^2 (p_{12} - \sigma (p_{11} + p_{12}))}{\beta_i} \right) \times \left(\frac{\iint n_0^4 |\psi_i|^2 dA}{\iint |\psi_i|^2 dA} \right) \left(\frac{T_{zz}}{Y} \right), \quad (22)$$

where p_{11} , p_{12} are the elasto-optic coefficients, σ is the Poisson ratio, and Y is the Young's modulus of fused silica.

Ulrich *et al.* previously showed that axial stress across a bent section of SMF induces a linear birefringence that is equal to [53]

$$\Delta b_i = \left(\frac{-k_0 n_0^3 (p_{11} - p_{12}) (1 + \sigma)}{4} \right) \left(\frac{a}{R} \right) \times \left(\frac{2(2 - 3\sigma)}{1 - \sigma} \right) \left(\frac{T_{zz}}{Y} \right), \quad (23)$$

where R is the radius of curvature and a is the outer radius of the fiber. We have simply adapted this relation to the MMF case.

Axial stress should contribute negligible mode coupling in an ideal straight fiber since the transverse index perturbation is axially symmetric and orthogonal modes stay uncoupled. However, since we have assumed an imperfect fiber with built-in mode coupling coefficients, axial stress can induce additional coupling. To account for this effect, we model

$$\Delta K_{ij} = \gamma K_{ij,0} T_{zz}, \quad (24)$$

where $\gamma = 0.01 \ll 1$ is a small fitting parameter, stemming from an intuitive argument that highly coupled modes are more affected by axial stress.

Axial stress also modifies the geometry of the fiber, as shown in Fig. 1. A fiber section of length Δl_0 under axial tension T_{zz} is stretched to a length [39]

$$\Delta l = \Delta l_0 \left(1 + \frac{T_{zz}}{Y} \right). \quad (25)$$

The core radius a also shrinks in response to the length elongation due to the Poisson effect. However, we ignore this here because it is a higher-order effect with a small impact on modal propagation.

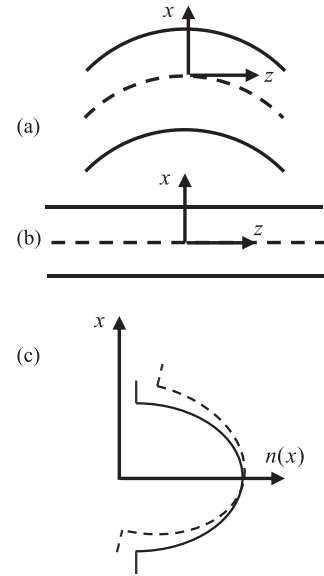


Fig. 2. The transformation of (a) bent MMF into (b) an equivalent straight MMF with (c) an index perturbation.

C. Modeling Local Bends

Fiber bends are difficult to model because they induce complicated stress fields and change the geometry of the waveguide. For simplicity of modeling, we consider bends in the x - z plane only with bending radius R .

Treating a SMF as a circular elastic rod, [53] first showed that bending induces birefringence between orthogonal polarizations because the outer portions of the fiber exert a second-order compressive stress on the inner layers. Reference [48] extended the analysis to the MMF case and showed that the induced birefringence is equal to

$$\Delta b_i = -\frac{\Omega^2 \mu_0 \epsilon_0 n_{av}^4}{4\beta_i} \left(\frac{a}{R} \right)^2 (1 + \sigma) (p_{12} - p_{11}). \quad (26)$$

Fiber bends also lead to mode coupling because the fiber is stretched on the outer side of the bend and compressed on the inner side. We use the method of refractive index transformation commonly used by authors in SMF literature [43] to convert a bent MMF with index profile n_0 into an equivalent straight MMF with a perturbed index profile n_s that is responsible for mode coupling (see Fig. 2). The effects of bends can be expressed as

$$n_s^2 = n_0^2 + n_p^2, \quad (27)$$

where n_p is the index perturbation that is a function of R . Considering the geometry of the bend and associated phase effects, [43] derived

$$n_p^2 \approx \frac{2 \cdot x \cdot n_0^2}{R}. \quad (28)$$

Substituting (28) into (8), we can derive the mode coupling coefficients due to bend as

$$\Delta K_{ij} = -\frac{j\Omega\epsilon_0 n_0^2}{2R} \iint x \psi_i^* \psi_j dA. \quad (29)$$

We observe that the above formula makes intuitive sense: modes are coupled by an index perturbation that varies linearly

along the transverse direction, and the magnitude of coupling is inversely proportional to the bend radius.

D. Modeling External Electromagnetic Fields

A transverse electric field E_{elec} introduces a linear birefringence between orthogonal polarization modes via the electro-optic Kerr effect. The amount of induced birefringence in SMF is equal to [54]

$$\Delta b_i = 2\pi B_K |E_{elec}|^2, \quad (30)$$

where B_K is the Kerr constant of fused silica. We have extended this relationship to the MMF case without assuming any mode-dependence to the amount of induced birefringence, which is an assumption that needs experimental verification.

Similarly, an axial magnetic field H_{mag} will yield circular birefringence and cause polarization coupling via the Faraday effect. The polarization coupling coefficient is given by [48], [54]

$$\Delta K_{ij} = V |H_{mag}|, \quad (31)$$

where V is the Verdet constant of fused silica and i and j are indices corresponding to different polarizations of the same spatial mode. Note that here too we have assumed all modes experience the same amount of polarization rotation due to the Faraday effect, which is another assumption that needs experimental verification.

IV. NUMERICAL MODELING OF AERIAL FIBER LINK

The goal of this section is to highlight the salient features of the model and showcase its ability to study equalizer tracking behavior in different regimes. Based on the model described in Sections II and III, we have performed numerical modeling of an example MMF aerial link that is subject to a sudden gust of wind. Section IV-A shows the static properties of the simulated aerial fiber link. Section IV-B describes our model for the induced stresses and vibrations in the aerial fiber caused by wind. Section IV-C discusses adaptive MIMO equalization using the LMS algorithm to track the effects of wind. Section IV-D shows simulation results of channel dynamics when the strength of wind, number of propagating modes, and length of aerial fiber are varied. Section IV-E discusses the tradeoffs in the choice of LMS equalization algorithm parameters.

A. Modeling an Aerial Fiber MDM Link

The fiber is a 6- μm graded-index graded-depressed cladding (GIGDC) fiber supporting $D = 6$ modes (see Fig. 4). This index profile is optimized for low uncoupled group delay (GD) spread, which is beneficial for long-haul MDM transmission, and the uncoupled GD spread decreases with an increasing number of modes [55]–[57]. The total length of the link is $L = 100$ km, composed of 30 km of static fiber, $L_H = 40$ km of active aerial fiber, and 30 km of static fiber, in that order. The fiber has a numerical aperture $NA = 0.15$ and the wavelength is $\lambda = 1550$ nm. The root-mean-square (rms) uncoupled GD spread is

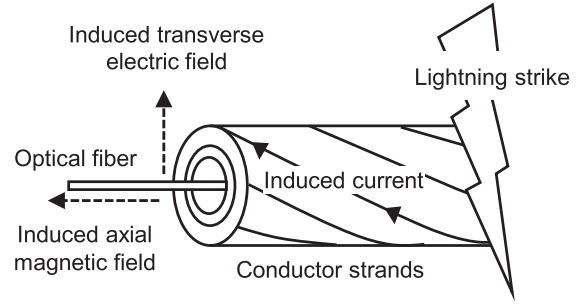


Fig. 3. Lightning strike near an optical ground wire containing transmission fiber.

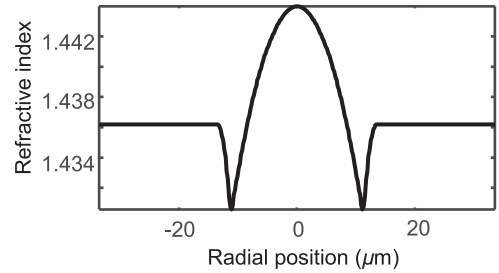


Fig. 4. GIGDC fiber index profile for $D = 6$ modes, which has been optimized for low group delay spread.

15 ps/km, and the mode-averaged CD parameter is 17 ps/nm/km. MDL is neglected in our simulations.

As evidenced in Fig. 5(a), the 6×6 transfer matrix $\mathbf{M}^a(\Omega, t)$ of the 40 km active section shows strong intragroup coupling in the LP_{01} and LP_{11} mode groups. Intergroup coupling between the two mode groups is very weak because the modes are not phase matched. Since we have neglected MDL in our simulations, $\mathbf{M}^a(\Omega, t)$ should be unitary, and we have indeed verified in Fig. 5(b) that $\mathbf{M}^a(\Omega, t) \cdot \mathbf{M}^a(\Omega, t)^H$ is a 6×6 identity matrix. Fig. 5(c) shows an overlay plot of all 36 impulse responses in the time domain, calculated from an inverse FFT of $\mathbf{M}^a(\Omega, t)$. The impulse responses belonging to the two mode groups are well separated in time as a result of modal dispersion.

B. Modeling a Sudden Gust of Wind

We analyze the effects on the transmission channel when wind suddenly impacts the 40-km section of aerial fiber. A realistic wind perturbation varies smoothly on a second to sub-second time scale, even though elements of the MDM channel can change on a microsecond time scale in response. As shown in Fig. 6, we focus on a concatenation of two discontinuous microsecond-time-scale intervals in our simulations. Interval A has negligible perturbation and allows the equalizer to converge, whereas interval B has a worst-case fast perturbation with a steep slope and tests equalizer tracking. Modeling a realistic perturbation as a time-domain ramp and simulating only a few microseconds of a much longer perturbation allows us to present equalizer convergence and tracking in the same plot (as in Figs. 8–10).

We assume that the aerial section is stable from $t = 0$ s until the wind starts at $t = 3 \mu\text{s}$. Once the wind starts, two main

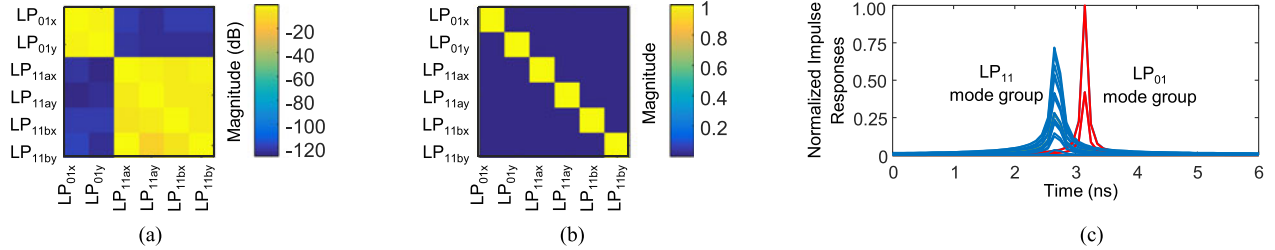


Fig. 5. Static properties of the aerial MMF supporting $D = 6$ modes. (a) Weak intergroup and strong intragroup coupling in the transfer matrix of the 40 km hinge section. (b) MIMO channel is unitary in absence of MDL. (c) Overlay of hinge time-domain impulse responses.

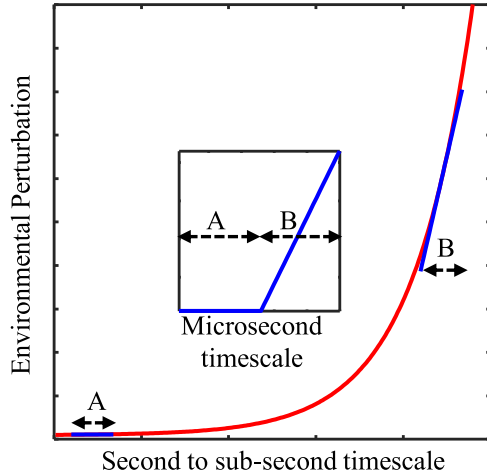


Fig. 6. Main plot: a realistic environmental perturbation, which varies smoothly on a second to subsecond time scale. Inset: perturbation used in our simulation, which is a concatenation of intervals A and B. Unperturbed interval A highlights initial equalizer convergence. Interval B, in which the perturbation varies rapidly, highlights equalizer tracking.

effects impact the MMF: (1) axial stress is induced inside the fiber, and (2) the fiber moves causing its position to relax from one distribution to another.

To model (1), we assume that a modest fraction of the fiber's tensile yield stress is induced inside the waveguide in a characteristic time scale of $\tau = 0.1$ s. The fiber yield stress, approximately $T_{zz,max} = 0.5$ GPa according to [58], [59], is the maximum axial stress that can be applied to the MMF in the regime of elasticity. Random spatially correlated tensile stresses, which are generated using a Langevin process with a correlation length of 20 m, stretch the fiber. In the worst case, $r = 1.5 \times 10^{-4}\%$ of the yield stress is induced into the fiber. Since the evolution of the wind is slow compared to the symbol rate of the receiver, the induced stresses are modeled as time-domain ramps. We again emphasize that the actual wind perturbation occurs on a sub-second time scale. The static interval (interval A in Fig. 6) has a duration of $3 \mu\text{s}$ and the active interval (interval B in Fig. 6) has a duration of $3 \mu\text{s}$ with a constant slope of

$$rT_{zz,max}/\tau = 1.5 \times 10^{-4}\% \times 0.5 \text{ GPa}/0.1 \text{ s} = 7500 \text{ Pa/s}. \quad (32)$$

Only a $6\text{-}\mu\text{s}$ time interval ($3 \mu\text{s}$ of a stable channel followed by $3 \mu\text{s}$ of a dynamic channel) is studied in this paper because it is sufficient to study channel dynamics and corresponding equalizer tracking behavior. The spatial distribution and time-

evolution of the axial stress is shown in Fig. 7. We note that our perturbative modeling should be valid because the stress magnitudes are very small.

To model (2), we assume that the fiber position shifts due to contact between the fiber jacket and its surroundings. The local curvatures of the MMF relax from one distribution to another in the same time scale as stress because the fiber bends in response to the wind. The initial curvatures, $\kappa_0(z) = 1/|R_0(z)|$, are sampled from the positive part of a normal distribution with a standard deviation of $1/2.5 \text{ m}^{-1}$. The curvatures 0.1 s later, $\kappa_1(z)$, are independently sampled from the same distribution. The local curvature at each z during the wind gust is linearly interpolated as

$$\kappa(z, t) = \kappa_0(z) + (\kappa_1(z) - \kappa_0(z)) \times (t/0.1). \quad (33)$$

Even though wind in a real setting might have additional effects beyond the simplified model we consider here, we show in Section IV-D that our model reproduces expected channel dynamics behavior.

C. Adaptive MIMO Equalization

The end-to-end transfer Jones matrix $\mathbf{M}(\Omega, t)$ represents time-varying mode coupling and dispersion, necessitating the use of an adaptive 6×6 MIMO equalizer \mathbf{W} at the receiver. For long-haul transmission, it is computationally efficient to transmit a CP to represent the MDM channel as circular convolution of discrete length sequences in the time-domain. This operation corresponds to multiplication in the discrete frequency domain, which can be efficiently realized by FFT processing in FDE. \mathbf{W} approximately inverts \mathbf{M} so the product $\mathbf{W}\mathbf{M}$ is approximately a 6×6 identity matrix. The convergence properties of several adaptive FDE algorithms were previously studied in [10]. Here, we focus on the tracking ability of the least mean squares (LMS) algorithm. LMS uses stochastic gradient descent to adapt to an unknown MIMO channel using estimates of the equalizer error. Since the feedforward carrier-recovery block has a delay of Δ samples, we use delayed outputs to adapt the coefficients of the LMS equalizer² [60].

²Lasers currently used in telecommunications have linewidths of the order of hundreds of kHz. Feedforward carrier recovery, often used for carrier phase recovery, employs filtering to average phase noise estimates. This filtering introduces a delay of tens to hundreds of samples (corresponding to several nanoseconds) between the equalizer outputs and computation of the error signals used to train the equalizer coefficients. The channel changes on a microsecond time scale, and our simulations show that the delay Δ causes a negligible increase in the equalizer MSE. All plots in this paper assume $\Delta = 0$ for simplicity.

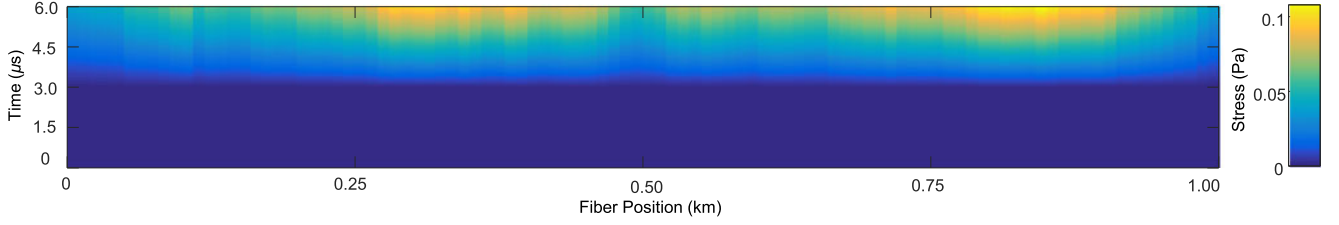


Fig. 7. Spatial and temporal distribution of the induced axial stress due to wind. Only 1 km active section is shown.

The coefficients of the 6×6 LMS equalizer at each discrete frequency $k = 0, 1, \dots, N_{FFT} - 1$ are iteratively updated as [10], [61]

$$\mathbf{W}[k] \leftarrow \mathbf{W}[k] + \mu(\tilde{\mathbf{x}}[k] - \mathbf{W}[k]\tilde{\mathbf{y}}[k])\tilde{\mathbf{y}}^H[k], \quad (34)$$

where μ is a scalar step size,

$$\begin{aligned} \tilde{\mathbf{x}}[k] &= [X_1[k], \dots, X_6[k]]^T \\ &= N_{FFT} - \text{point FFT} \\ &\text{of delayed time domain signals } \mathbf{x}[n - \Delta] \end{aligned} \quad (35)$$

is a block of known or estimated frequency domain data symbols that were transmitted,

$$\begin{aligned} \tilde{\mathbf{y}}[k] &= \mathbf{M}[k]\tilde{\mathbf{x}}[k] + \tilde{\mathbf{n}}[k] \\ &= [Y_1[k], \dots, Y_6[k]]^T \\ &= N_{FFT} - \text{point FFT} \\ &\text{of delayed time domain signals } \mathbf{y}[n - \Delta] \end{aligned} \quad (36)$$

is a block of received frequency-domain symbols at the input of the equalizer, and $\tilde{\mathbf{n}}[k] = [N_1[k], \dots, N_6[k]]^T$ is a block of noise samples. The convergence rate and performance of the LMS algorithm depend on the choice of μ which must satisfy the convergence criterion $0 < \mu < 2/\lambda_{max}$. Here λ_{max} is the largest eigenvalue of the autocovariance matrix of $\tilde{\mathbf{y}}[k]$, $R_{\tilde{\mathbf{y}}}[k] = E\{\tilde{\mathbf{y}}[k]\tilde{\mathbf{y}}[k]^H\}$ [10]. The squared error in the equalized samples at each discrete frequency k is computed as $\epsilon^2[k] = \|\tilde{\mathbf{x}}[k] - \mathbf{W}[k]\tilde{\mathbf{y}}[k]\|^2$, and we compute a normalized mean-squared error (MSE) by ensemble averaging the squared error over all N_{FFT} discrete-frequencies, all modes, and many realizations of the transmitted data symbols $\mathbf{x}[n]$.

In our simulation, both polarizations of the LP_{01} and LP_{11} mode groups are launched at the transmitter and all six modes are detected with a coherent MIMO receiver which is operating at a symbol rate of $R_s = 20$ Gbaud. Random quadrature phase-shift keying training data $\mathbf{x}[n]$ is sent on each mode and $\mathbf{y}[n]$ is detected at a signal-to-noise ratio (SNR) of 15 dB. The SNR is defined as the received signal power over all six modes divided by the received noise power per mode. The LMS equalizer has a step size of $\mu = 0.05$ and a FFT block size of $N_{FFT} = 2^9$.

D. Simulation Results of Aerial Fiber Dynamics

We now study the channel dynamics of the aerial fiber link and tracking performance of LMS-adapted MIMO FDE, and their dependence on the strength of the wind perturbation, number of modes, and the length of the hinge. In each comparison,

the default parameters are $D = 6$ modes and hinge length is $L_H = 40$ km. The default wind perturbation stretches the fiber from 0% to $1.5 \times 10^{-4}\%$ of the yield strength and shifts the local curvatures from one distribution to another in 0.1 s. The LMS algorithm step size is fixed at $\mu = 0.05$ and the block size $N_{FFT} = 2^9$ for all cases considered here.

Figs. 8–10(a)–(c) show the evolution of elements in the received Jones vector at the carrier frequency $\tilde{\mathbf{y}}[k = 0]$ when a fixed Jones vector $\tilde{\mathbf{x}}[k = 0]$ is transmitted. The elements of $\tilde{\mathbf{y}}$ remain stable until $t = 3 \mu\text{s}$, when the wind perturbation is turned on. Increasing axial stress and shifting curvatures cause time-varying mode coupling, as evidenced by change in the received Jones vector elements. Even though the wind perturbation happens only in the sub-second time scale, we observe microsecond-time-scale channel dynamics, consistent with initial experimental observations [6]. The equalizer starts without an initial estimate of the fiber channel and so its weights are initialized to 0 at $t = 0$ s. The equalizer begins learning the static fiber channel and its weights converge to the optimum values around $t = 1.5 \mu\text{s}$. When the wind starts, the equalizer changes from convergence mode to tracking mode. Its weights track the time-varying modal dispersion and mode coupling as a function of the scalar step size μ (discussed further in Section IV-E). The evolution of the diagonal coefficients of the MIMO equalizer are shown in Figs. 8–10(d)–(f). For clarity, only the diagonal weights of the equalizer are shown. Figs. 8–10(g) show equalizer learning performance in terms of normalized MSE during initial convergence and subsequent tracking.

Fig. 8 shows the channel dynamics and equalizer tracking behavior when the strength of the wind acting on the aerial fiber is varied. The wind perturbations in Fig. 8(b), (e) and (c), (f) are two and four times as strong as in Fig. 8(a) and (d), respectively. As expected, the received Jones vector elements evolve faster with increasing perturbation strength. The LMS equalizer converges around $t = 1.5 \mu\text{s}$ for all three cases, yielding an asymptotic normalized MSE around 0.01. When the wind starts at $t = 3 \mu\text{s}$, the channels become dynamic and the instantaneous normalized MSE increases to 0.03, 0.07, and 0.21 for the three wind strengths, suggesting a super-linear scaling of the MSE with the strength of perturbation.

Fig. 9 shows how the channel dynamics and equalizer tracking performance change when D is varied. The received Jones vector elements of an aerial cable using MMF ($D = 6, 12$) evolve faster than those of an aerial cable using SMF ($D = 2$). As the dimensionality of the system increases, the complex dynamics of mode coupling and dispersion make it more difficult for the equalizer to track the MIMO channel, as evidenced by the higher

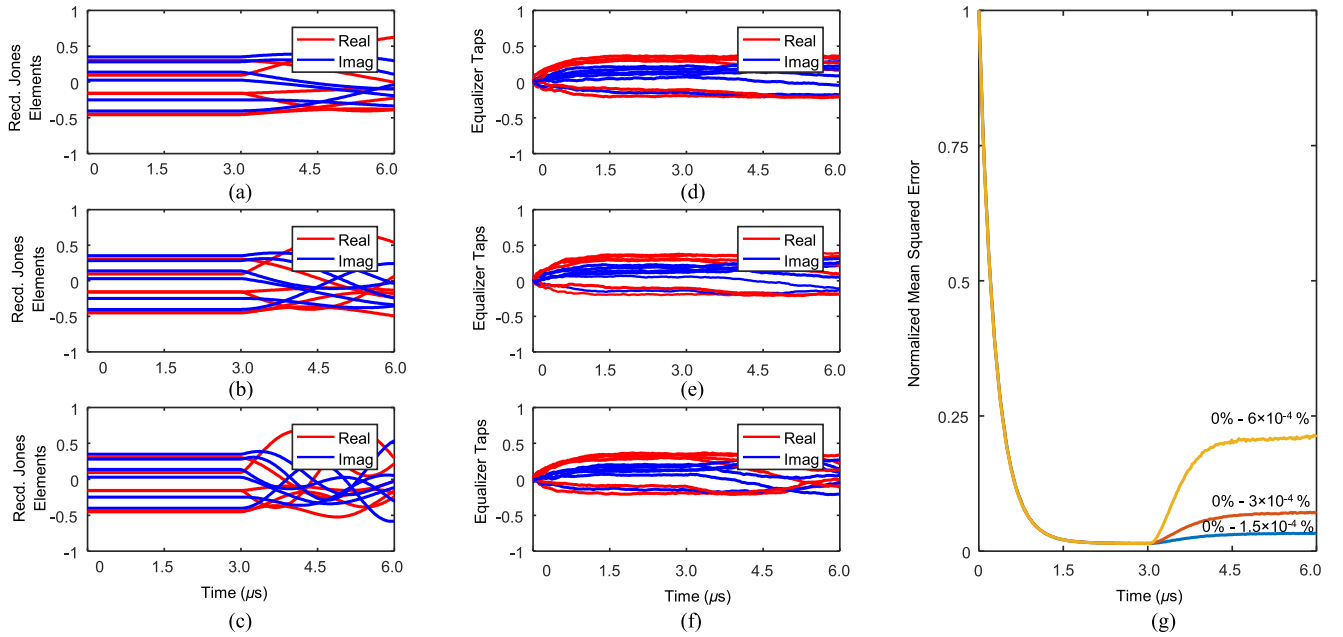


Fig. 8. Received Jones vector elements for a random transmitted Jones vector for $D = 6$ modes, LMS equalizer diagonal taps with $\mu = 0.05$ when the axial stress is ramped from (a), (d) 0% to $1.5 \times 10^{-4}\%$, (b), (e) 0% to $3 \times 10^{-4}\%$, and (c), (f) 0% to $6 \times 10^{-4}\%$ of fiber yield stress within 0.1 s. The distribution of curvatures in (b), (e) and (c), (f) is changing two times and four times faster than in (a) and (d), respectively. The corresponding MSE curves are shown in (g).

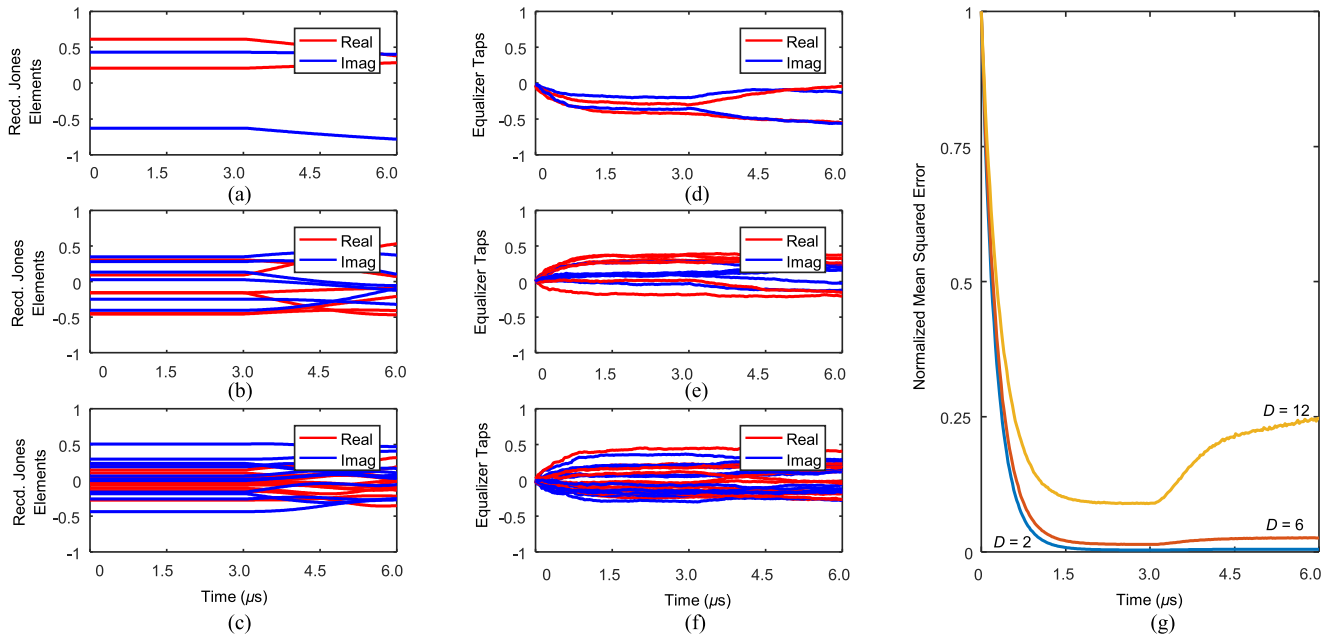


Fig. 9. Received Jones vector elements for a random transmitted Jones vector and LMS equalizer diagonal taps with $\mu = 0.05$ when the axial stress is ramped from 0% to $1.5 \times 10^{-4}\%$ of fiber yield strength and local curvatures are changing within 0.1 s for (a), (d) $D = 2$ modes, (b), (e) $D = 6$ modes, and (c), (f) $D = 12$ modes. The corresponding MSE curves are shown in (g).

instantaneous MSE for MMFs as compared to SMF, which is shown in Fig. 9(g).

While MMF channels have been observed to change faster than SMF channels, as shown in [6] and later references, the underlying physical reasons for the increased rate of change are not entirely clear. Within our model based on coupled-mode theory, it is the matrices $\Gamma(\Omega, t)$ and $\mathbf{K}(\Omega, t)$, which appear in the exponent of the transfer matrix $\mathbf{M}(\Omega, t)$ (see, e.g., (14)), that are

responsible for all linear effects. As D increases, a given external force causes the pairwise coupling coefficients in $\mathbf{K}_d(\Omega, t)$ to change faster; higher-order modes tend to overlap more than lower-order modes, so the overlap integrals describing the pairwise coupling coefficients are more sensitive to changes in the index perturbation. While this reasoning is not yet validated experimentally, the predictions of our model are consistent with experimental observations.

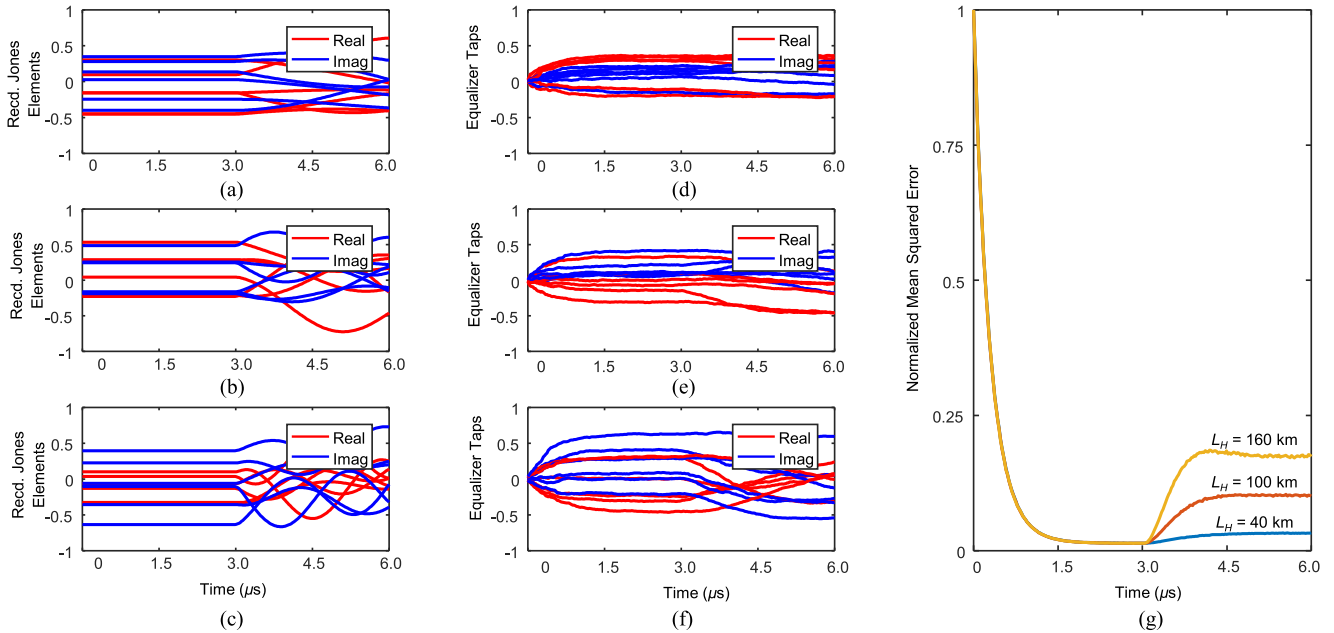


Fig. 10. Received Jones vector elements for a random transmitted Jones vector for $D = 6$ modes and LMS equalizer diagonal taps with $\mu = 0.05$ when the axial stress is ramped from 0% to $1.5 \times 10^{-4}\%$ of fiber yield strength and local curvatures are changing within 0.1 s for hinge length (a), (d) $L_H = 40$ km, (b), (e) $L_H = 100$ km, and (c), (f) $L_H = 160$ km. The corresponding MSE curves are shown in (g).

Fig. 10 shows a similar comparison, namely, how the channel dynamics and equalizer tracking performance change when the length of the aerial fiber exposed to the wind is varied. As expected, longer exposed fiber lengths cause faster channel dynamics, because the end-to-end Jones transfer matrix represents the cumulative effects of local mode coupling and dispersion integrated along the fiber length. Consequently, tracking dynamic channels with longer fiber lengths can yield higher instantaneous MSE, as shown in Fig. 10(g).

Figs. 8–10 empirically show the effect of varying different parameters on MDM channel dynamics and the output MSE of the equalizer. It is of significant practical interest to develop insightful metrics to quantify the rate of change of a MIMO channel, explain their dependence on system parameters, and establish a connection to the output MSE of the adaptive MIMO equalizer.

Channel dynamics in SMF, with $D = 2$ modes, are often described in terms of rotations per second of the received Stokes vector on the Poincaré sphere. In these low-dimensional systems, higher rotation rates are correlated with increased difficulty of tracking by an adaptive equalizer. Moreover, the rotation rate is easy to measure using polarimeters in a laboratory setting, and consequently this metric has become the optical communications industry's *de facto* metric for quantifying channel rate of change. However, a simple extension of this idea for $D > 2$ modes to rotations of the generalized Stokes vector on the generalized Poincaré sphere can be non-physical. Not all vectors on the generalized Poincaré sphere have a legitimate representation as a generalized Jones vector [16]. Moreover, generalized Stokes vectors are constructed from their generalized Jones vector counterparts using trace-orthogonal basis Pauli matrices, which are not unique.

Given these complications, it is hard to relate rotations on the generalized Poincaré sphere to output MSE of the adaptive MIMO equalizer. Nevertheless, determining if rotation rate of the generalized Stokes vector has useful meaning or developing other, more useful, metrics to quantify the rate of MDM channel change is an important subject for future research.

E. Optimization of LMS Equalization Algorithm Parameters

The tracking performance of the LMS FDE algorithm is a strong function of its step size and FFT block length. In this section, we vary these parameters to study the effect on the instantaneous MSE.

The choice of μ has an important system design tradeoff: it should be chosen large enough to allow the weights to faithfully track dynamic channels, but small enough to avoid excess mean squared error (MSE) in stable channels. As shown in Fig. 11, small values for μ yield the smallest asymptotic MSE when the channel is stable but result in slow tracking of channel dynamics. High values for μ result in excess MSE when the link is stable due to noisy equalizer updates but are capable of tracking dynamics faithfully [62]. Considering this tradeoff, $\mu = 0.05$ is a reasonable choice for the example system considered here. In practice, μ is often adjusted empirically to optimize performance.

Since the LMS-adapted FDE is iteratively updated using received blocks of N_{FFT} samples of $D \times 1$ vectors, successive LMS updates must equalize changes to the Jones transfer matrix that have occurred in the past N_{FFT} samples. The change to the transfer matrix that is seen by the equalizer is proportional to both the rate of channel dynamics and N_{FFT} , which means that the tracking ability of the equalizer is reduced as N_{FFT} is

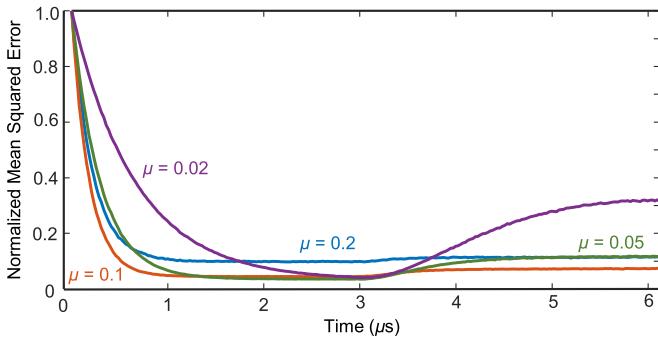


Fig. 11. Tracking performance of the LMS FDE algorithm for various values of the step size parameter μ . Over a time interval of 0.1 s, the axial stress is ramped from 0% to 1.5×10^{-4} % of fiber yield strength, and the local curvatures are changed. The MMF supports $D = 6$ modes and the length of the aerial hinge is $L_H = 40$ km.

increased. However, long-haul MDM systems have a large group delay spread, which requires a large CP. The requirement of a high CP efficiency to increase throughput puts a lower bound on the N_{FFT} that can be employed.

V. CONCLUSION

We have extended the multi-section model to describe how spatial- and polarization- mode coupling in MMFs change in response to fast environmental perturbations. Our model is able to compute the time-varying Jones transfer matrix of an end-to-end MDM link when given the distributions of the environmental perturbations that are acting upon it. The essence of our model is to assume that a MMF has built-in defects originating from manufacturing and cabling that reproduce the expected behavior of mode coupling and dispersion when the link is stable.

The driving environmental perturbations, including axial stress, curvature and external electromagnetic fields, modulate the fiber properties to produce time-varying mode-dependent phase shifts, mode coupling, and modal dispersion in a dynamic channel. We have shown that the rate of channel dynamics can be in the microsecond time scale even though the time scale for the environmental dynamics is much slower, e.g., on the sub-second time scale. The MDM channel evolves faster as D is increased because external forces can potentially impose stronger and faster changes to the mode coupling coefficient matrix. Increasing the hinge length of an MDM link also increases the rate of dynamics because distributed perturbations can interact with the channel over a longer length.

The increased speed of channel dynamics with increasing number of modes D or link length can potentially have a critical impact on adaptive MIMO equalization in long-haul MDM systems. Adaptive equalizers need to be designed so that they can track the fastest channel variations. However, there is an inherent tradeoff in the tracking ability in dynamic channels and the asymptotic MSE in static channels. The long group-delay spread necessitates a large CP length, and a high CP efficiency requires a large N_{FFT} , but large N_{FFT} slows down equalizer tracking and lead to higher MSE when the channel changes rapidly.

REFERENCES

- [1] T. Morioka *et al.*, "Enhancing optical communications with brand new fibers," *IEEE Commun. Mag.*, vol. 50, no. 2, pp. s31–s42, Feb. 2012.
- [2] E. Ip, G. Milione, Y.-K. Huang, and T. Wang, "Impact of mode-dependent loss on long-haul transmission systems using few-mode fibers," in *Proc. Opt. Fiber Commun. Conf. Exhib.*, 2016, pp. 1–3.
- [3] P. M. Krummrich and K. Kotten, "Extremely fast (microsecond timescale) polarization changes in high speed long haul WDM transmission systems," in *Proc. Opt. Fiber Commun. Conf. Exhib.*, 2004, p. 1–3.
- [4] K. Roberts *et al.*, "Performance of dual-polarization QPSK for optical transport systems," *J. Lightw. Technol.*, vol. 27, no. 16, pp. 3546–3559, Aug. 2009.
- [5] M. Boroditsky *et al.*, "Polarization dynamics in installed fiberoptic systems," in *Proc. IEEE LEOS Annu. Meeting*, 2005, pp. 414–415.
- [6] X. Chen *et al.*, "Characterization and analysis of few-mode fiber channel dynamics," *IEEE Photon. Technol. Lett.*, vol. 25, no. 18, pp. 1819–1822, Sep. 2013.
- [7] K. Ogaki, M. Nakada, Y. Nagao, and K. Nishijima, "Fluctuation differences in the principal states of polarization in aerial and buried cables," in *Proc. Opt. Fiber Commun. Conf.*, 2003, pp. 14–15.
- [8] M. Brodsky *et al.*, "Physical mechanism for polarization mode dispersion temporal dynamics," *IEEE LEOS Newslett.*, vol. 18, no. 3, pp. 4–6, 2004.
- [9] K. Choutagunta and J. M. Kahn, "Dynamic channel modeling for mode-division multiplexing," in *Proc. IEEE Photon. Soc. Summer Top. Space-Division Multiplex Multimode Photon.*, Newport Beach, CA, USA, Jul. 11–13, 2016, pp. 49–50.
- [10] S. Ö. Arık, D. Askarov, and J. M. Kahn, "Adaptive frequency-domain equalization in mode-division multiplexing systems," *J. Lightw. Technol.*, vol. 32, no. 10, pp. 1841–1852, May 2014.
- [11] S. Ö. Arık, D. Askarov, and J. M. Kahn, "Effect of mode coupling on signal processing complexity in mode-division multiplexing," *J. Lightw. Technol.*, vol. 31, no. 3, pp. 423–431, Feb. 2013.
- [12] C. D. Poole, "Statistical treatment of polarization dispersion in single-mode fiber," *Opt. Lett.*, vol. 13, pp. 687–689, 1988.
- [13] C. D. Poole and R. E. Wagner, "Phenomenological approach to polarisation dispersion in long single-mode fibres," *Electron. Lett.*, vol. 22, pp. 1029–1030, 1986.
- [14] J. P. Gordon and H. Kogelnik, "PMD fundamentals: Polarization mode dispersion in optical fibers," *Proc. Nat. Acad. Sci.*, vol. 97, pp. 4541–4550, 2000.
- [15] C. Antonelli, A. Mecozzi, M. Shtaf, and P. J. Winzer, "Random coupling between groups of degenerate fiber modes in mode multiplexed transmission," *Opt. Express*, vol. 21, pp. 9484–9490, 2013.
- [16] C. Antonelli, A. Mecozzi, M. Shtaf, and P. J. Winzer, "Stokes-space analysis of modal dispersion in fibers with multiple mode transmission," *Opt. Express*, vol. 20, pp. 11718–11733, 2012.
- [17] J. Schuster, Z. Marzec, W. L. Kath, and G. Biondini, "Hybrid hinge model for polarization-mode dispersion in installed fiber transmission systems," *J. Lightw. Technol.*, vol. 32, no. 7, pp. 1412–1419, Apr. 2014.
- [18] J. Li, G. Biondini, W. L. Kath, and H. Kogelnik, "Anisotropic hinge model for polarization-mode dispersion in installed fibers," *Opt. Lett.*, vol. 33, pp. 1924–1926, 2008.
- [19] J. Li, G. Biondini, W. L. Kath, and H. Kogelnik, "Outage statistics in a waveplate hinge model of polarization-mode dispersion," *J. Lightw. Technol.*, vol. 28, no. 13, pp. 1958–1968, Jul. 2010.
- [20] C. Antonelli and A. Mecozzi, "Theoretical characterization and system impact of the hinge model of PMD," *J. Lightw. Technol.*, vol. 24, no. 11, pp. 4064–4074, Nov. 2006.
- [21] D. S. Waddy, L. Chen, and X. Bao, "Theoretical and experimental study of the dynamics of polarization-mode dispersion," *IEEE Photon. Technol. Lett.*, vol. 14, no. 4, pp. 468–470, Apr. 2002.
- [22] A. Mecozzi, C. Antonelli, M. Boroditsky, and M. Brodsky, "Characterization of the time dependence of polarization mode dispersion," *Opt. Lett.*, vol. 29, pp. 2599–2601, 2004.
- [23] C. B. Czegledi, M. Karlsson, E. Agrell, and P. Johansson, "Polarization drift channel model for coherent fibre-optic systems," *Sci. Rep.*, vol. 6, 2016, Art. no. 21217.
- [24] M. Brodsky, N. J. Frigo, M. Boroditsky, and M. Tur, "Polarization mode dispersion of installed fibers," *J. Lightw. Technol.*, vol. 24, no. 12, pp. 4584–4599, Dec. 2006.
- [25] G. Soliman, "Temporal dynamics of polarization and polarization mode dispersion and influence on optical fiber systems," Ph.D. dissertation, Univ. Waterloo, Waterloo, ON, Canada, 2013.

- [26] R. Roberge, "Case study: PMD measurement on aerial fiber under wind-induced oscillations and vibration," 2009. [Online]. Available: <http://metrotek.ru/>
- [27] M. Belloli, A. Collina, and F. Resta, "Cables vibration due to wind action," 2006. [Online]. Available: <http://www.oitaf.org/>
- [28] M. Kurono, K. Isawa, and M. Kuribara, "Transient state of polarization in optical ground wire caused by lightning and impulse current," *Proc. SPIE*, vol. 2873, pp. 242–245, 1996.
- [29] S. M. Pietralunga, J. Colombelli, A. Fellegara, and M. Martinelli, "Fast polarization effects in optical aerial cables caused by lightning and impulse current," *IEEE Photon. Technol. Lett.*, vol. 16, no. 11, pp. 2583–2585, Nov. 2004.
- [30] J. G. Rose, D. M. Durrett, L. A. Walker, and J. C. Stith, "Highway-railway at-grade crossings: Trackbed and surface pressure measurements and assessments," 2009. [Online]. Available: <http://uknowledge.uky.edu/>
- [31] T. G. Gutowski and C. L. Dym, "Propagation of ground vibration: A review," *J. Sound Vib.*, vol. 49, pp. 179–193, 1976.
- [32] M. Brodsky, J. C. Martinez, N. J. Frigo, and A. Sirenko, "Dispersion compensation module as a polarization hinge," in *Proc. 31st Eur. Conf. Opt. Commun.*, Sep. 2005, pp. 335–336.
- [33] Cisco, "Data center power and cooling," 2017. [Online]. Available: http://www.cisco.com/c/en/us/solutions/collateral/data-center-virtualization/unified-computing/white_paper_c11-680202.pdf
- [34] D. Marcuse, *Theory of Dielectric Optical Waveguides*, 2nd ed. New York, NY, USA: Academic, 1991.
- [35] J. N. Damask, *Polarization Optics in Telecommunications*. New York, NY, USA: Springer-Verlag, 2005.
- [36] J. Proakis and M. Salehi, *Digital Communications*, 5th ed. New York, NY, USA: McGraw-Hill, 2007.
- [37] R. Olshansky, "Mode coupling effects in graded-index optical fibers," *Appl. Opt.*, vol. 14, pp. 935–945, 1975.
- [38] S. Ö. Arık and J. M. Kahn, "Coupled-core multi-core fibers for spatial multiplexing," *IEEE Photon. Technol. Lett.*, vol. 25, no. 21, pp. 2054–2057, Nov. 2013.
- [39] C.-L. Chen, *Foundations for Guided-Wave Optics*. New York, NY, USA: Wiley-Interscience, 2006.
- [40] A. Li, Y. Wang, Q. Hu, and W. Shieh, "Few-mode fiber based optical sensors," *Opt. Express*, vol. 23, pp. 1139–1150, 2015.
- [41] T. Hayashi *et al.*, "Crosstalk variation of multi-core fibre due to fibre bend," in *Proc. Eur. Conf. Opt. Commun.*, 2010, pp. 1–3.
- [42] H. Bülow, H. Al-Hashimi, B. T. Abebe, and B. Schmauss, "Capacity and outage of multimode fiber with statistical bends," in *Proc. Opt. Fiber Commun. Conf. Expo./Nat. Fiber Optic Eng. Conf.*, 2012, pp. 1–3.
- [43] A. A. Juárez *et al.*, "Modeling of mode coupling in multimode fibers with respect to bandwidth and loss," *J. Lightw. Technol.*, vol. 32, no. 8, pp. 1549–1558, Apr. 2014.
- [44] P. M. Krummrich *et al.*, "Demanding response time requirements on coherent receivers due to fast polarization rotations caused by lightning events," *Opt. Express*, vol. 24, pp. 12442–12457, 2016.
- [45] J. Wuttke, P. M. Krummrich, and J. Rosch, "Polarization oscillations in aerial fiber caused by wind and power-line current," *IEEE Photon. Technol. Lett.*, vol. 15, no. 6, pp. 882–884, Jun. 2003.
- [46] M. Brodsky, P. Magill, and N. J. Frigo, "Polarization-mode dispersion of installed recent vintage fiber as a parametric function of temperature," *IEEE Photon. Technol. Lett.*, vol. 16, no. 1, pp. 209–211, Jan. 2004.
- [47] R. Ulrich and A. Simon, "Polarization optics of twisted single-mode fibers," *Appl. Opt.*, vol. 18, pp. 2241–2251, 1979.
- [48] L. Palmieri and A. Galtarossa, "Coupling effects among degenerate modes in multimode optical fibers," *IEEE Photon. J.*, vol. 6, no. 6, 2014, Art. no. 0600408.
- [49] M. V. Berry, "Interpreting the anholonomy of coiled light," *Nature*, vol. 326, pp. 277–278, 1987.
- [50] M. V. Berry, "The adiabatic phase and Pancharatnam's phase for polarized light," *J. Modern Opt.*, vol. 34, pp. 1401–1407, 1987.
- [51] M. Plöschner, T. Tyc, and T. Čížmár, "Seeing through chaos in multimode fibres," *Nature Photon.*, vol. 9, pp. 529–535, 2015.
- [52] J. N. Blake, S. Y. Huang, B. Y. Kim, and H. J. Shaw, "Strain effects on highly elliptical core two-mode fibers," *Opt. Lett.*, vol. 12, pp. 732–734, 1987.
- [53] R. Ulrich, S. C. Rashleigh, and W. Eickhoff, "Bending-induced birefringence in single-mode fibers," *Opt. Lett.*, vol. 5, pp. 273–275, 1980.
- [54] S. Rashleigh, "Origins and control of polarization effects in single-mode fibers," *J. Lightw. Technol.*, vol. LT-1, no. 2, pp. 312–331, Jun. 1983.
- [55] D. Donlagic, "Opportunities to enhance multimode fiber links by application of overfilled launch," *J. Lightw. Technol.*, vol. 23, no. 11, pp. 3526–3540, Nov. 2005.
- [56] K. Okamoto and T. Okoshi, "Computer-aided synthesis of the optimum refractive-index profile for a multimode fiber," *IEEE Trans. Microw. Theory Techn.*, vol. MTT-25, no. 3, pp. 213–221, Mar. 1977.
- [57] K. Takahashi, T. Ishigure, and Y. Koike, "Index profile design for high-bandwidth W-shaped plastic optical fiber," *J. Lightw. Technol.*, vol. 24, no. 7, pp. 2867–2876, Jul. 2006.
- [58] *Corning Smf-28 Optical Fiber*, Corning Inc., Corning, NY, USA, 2002.
- [59] R. Romaniuk, "Tensile strength of tailored optical fibers," *Opto-Electron. Rev.*, vol. 8, no. 2, pp. 101–116, 2000.
- [60] E. Ip and J. M. Kahn, "Feedforward carrier recovery for coherent optical communications," *J. Lightw. Technol.*, vol. 25, no. 9, pp. 2675–2692, Sep. 2007.
- [61] S. Randel *et al.*, " 6×56 -Gb/s mode-division multiplexed transmission over 33-km few-mode fiber enabled by 6×6 MIMO equalization," *Opt. Express*, vol. 19, pp. 16697–16707, 2011.
- [62] B. Widrow and S. D. Stearns, *Adaptive Signal Processing*. Englewood Cliffs, NJ, USA: Prentice-Hall, 1985.

Karthik Choutagunta (S'11) received the B.S. degree from the University of Texas at Austin, TX, USA, in 2014, and the M.S. degree in electrical engineering in 2016 from Stanford University, Stanford, CA, USA, where he is currently working toward the Ph.D. degree. He worked at Coherent Logix, Austin, in Summer 2012, at Intel Corp., Austin, from 2012 to 2014, and at Apple Inc., Cupertino, CA, in Fall 2015 and Summer 2016. His main current research interests include various topics in optical communications, wireless communications, and signal processing.

Joseph M. Kahn (M'90–SM'98–F'00) received the A.B., M.A., and Ph.D. degrees in physics from the University of California, Berkeley (UC Berkeley), CA, USA, in 1981, 1983, and 1986, respectively. From 1987 to 1990, he was at AT&T Bell Laboratories, Crawford Hill Laboratory, Holmdel, NJ, USA. He demonstrated multi-Gbit/s coherent optical fiber transmission systems, setting world records for receiver sensitivity. From 1990 to 2003, he was with the Faculty of the Department of Electrical Engineering and Computer Sciences, UC Berkeley, performing research on optical and wireless communications. Since 2003, he has been a Professor of electrical engineering at Stanford University, Stanford, CA, where he heads the Optical Communications Group. His current research interests include fiber-based imaging, spatial multiplexing, rate-adaptive and spectrally efficient modulation and coding methods, coherent detection and associated digital signal processing algorithms, digital compensation of fiber nonlinearity, and free-space systems. He received the National Science Foundation Presidential Young Investigator Award in 1991. From 1993 to 2000, he served as a Technical Editor of *IEEE Personal Communications Magazine*. Since 2009, he has been an Associate Editor of the *IEEE/OSA JOURNAL OF OPTICAL COMMUNICATIONS AND NETWORKING*. In 2000, he helped found StrataLight Communications, where he served as the Chief Scientist from 2000 to 2003. StrataLight was acquired by Opnext, Inc., in 2009.